Received: 21 June 2017 | Revised: 4 October 2017 | Accepted: 21 November 2017

DOI: 10.1002/htj.21331

WILEY

RESEARCH ARTICLE

Flow control with electrode bank arrangements by electrohydrodynamics force for heat transfer enhancement in a porous medium

Suwimon Saneewong Na Ayuttaya[1] | Chainarong Chaktranond[2] | Phadungsak Rattanadecho[3]

[1]Department of Mechanical Engineering, Academic Division, Chulachomklao Royal Military Academy, Muang, Nakhon-Nayok, Thailand

[2]Department of Mechanical Engineering, Faculty of Engineering, Thammasat University, Khlong Luang, Pathum Thani, Thailand

[3]Department of Mechanical Engineering, Center of Excellence in Electromagnetic Energy Utilization in Engineering (CEEE), Faculty of Engineering, Thammasat University, Khlong Luang, Pathum Thani, Thailand

Correspondence
Suwimon Saneewong Na Ayuttaya, Department of Mechanical Engineering, Academic Division, Chulachomklao Royal Military Academy, Nakhon-Nayok, Thailand 26001.
Email: joysuwimon1@hotmail.com

Abstract

Active flow control with electrohydrodynamics (EHD) force in the channel flow has been numerically investigated for enhancing heat transfer. This study focuses on the effect of electrode bank arrangements and the number of electrodes on corona wind and fluid flow for heat transfer onto a porous medium. Aligned and staggered configurations of electrode banks are compared. The numerical results show that electric field intensity depends on electrical voltage and the number of electrodes. Shear flow is increased with larger numbers of electrodes and in the aligned configuration, resulting in the enhancement of vortex strength. The swirling flow from staggered configurations spread wider than that of aligned configurations, but the aligned configuration produced more turbulence. In addition, the

Nomenclature: A, area (m^2); b, ion mobility ($m^2/V.s$); C, electricity capacity (C/V); C_p, specific heat (J/K); D, electric flux density (C/m^2); d, displacement between electrode and ground (cm); E, electric field (V/m); EHD, Electrohydrodynamics; f_E, electric force or Coulomb force (C/m^2s); H, height of channel (m) and length of electrode wire (cm); h, gap in the vertical direction (cm); I, identity matrix; J, current density (A/m^2); k, thermal conductivity ($W/m.K$); L, length of channel (m); l, gap in the horizontal direction (cm); n, number of electrodes and unit vector and coordinate in x and y axis; P, pressure (N/m^2), porous medium sample; Q, charge density (C); q, space charge density (C/m^3); u, inlet velocity (m/s); V, electrical voltage (V); $\forall$, volume (m^3); T_α, ambient temperature (K); h_c, convective heat transfer coefficient (W/m^2K); Nu, augmented heat transfer (-); T, uniform temperature (K); t, time (hr); x, y, axis

Greek Symbols: α, thermal diffusivity (W/mK); ε, dielectric permittivity (F/m); κ, permittivity m^2; η, kinematics viscosity (m^2/s); μ, viscosity ($kg/m\,s$); ρ, density (kg/m^3); ϕ, porosity ($-$)

Subscripts: d, lower; u, upper; 0, atmospheric and wire; eff, effective; i, inlet; l, liquid; s, solid

Superscript: T, transpose of matrix

temperature distribution in the channel flow is increased with increasing numbers of electrodes. With the effect of swirling flow, airflow above the porous sample surface is faster leads the heat to more transfer to the porous sample surface. This causes the temperature of porous medium to increase rapidly so the convective heat transfer coefficient on porous medium surface is increased. Finally, the modified case of the numerical results is validated against the experimental results. The experimental flow visualization is based on the incense smoke technique, in order to verify the accuracy of the swirling flow pattern subjected to the electric field. It is shown that the comparison results in both techniques are in good agreement.

KEYWORDS

electrode bank arrangements, heat transfer enhancement, number of electrodes, porous medium, shear flow

1 | INTRODUCTION

Flow control is an emerging field of fluid dynamics which is being exploited to improve the performance of aerodynamic surfaces under widely varying conditions. Flow control is one of the leading areas of research for many scientists and engineers in fluid mechanics. Technology advances in the field enable data to be handled at an efficient pace.[1,2] The active flow and passive flow are two types of flow control. Passive control devices are always in operation, regardless of need or performance penalty. Active flow control, on the other hand, involves adding energy or momentum to flow in a regulated manner. Active flow control is more desirable than passive flow control because flow can be manipulated under various required conditions, but active flow control also involves additional effort and cost. Actuators are at the heart of active flow control implementation but have also been the weakest link in the development of flow control technology. The desired attributes of actuators include light weight, low profile, no moving parts, energy efficiency and durability, ease of use, scalability, high amplitude, wide bandwidth, and rapid response. Electrohydrodynamics (EHD) methods are one type of active flow control. EHD is the study of the mechanics of electrically charged fluids. It is the study of the motion of ionized particles or molecules and their interactions with electric fields and the surrounding fluid. The term may be considered to be synonymous with electrostrictive hydrodynamics. EHD covers the following types of particle and fluid transport mechanisms: electrophoresis, electrokinesis, and dielectrophoresis.[3] In general, the phenomena relate to the direct conversion of electrical energy into kinetic energy. First, ionic wind mechanism or Coulomb force mechanism is presented by Yabe and colleagues (1978).[4] A theoretical analysis had been conducted based on the model that positive ions produced by ionization near the wire electrode moved toward the plate, introducing the bulk convective motion of neutral molecules as the result of collisions of ions and neutral molecules. Consequently, it is made clear that the corona wind was caused by the Coulomb force exerted on ions and collisions of ions and neutral molecules of gas. Mechanism of EHD method is presented by Saneewong Na Ayuttaya and colleagues.[5] When electrical voltage is exposed to airflow, the airflow is created by ions generated in the corona discharge near the sharp electrode that drift to the ground. As a result, the momentum of airflow is enhanced and cross-flow or primary flow is generated. The primary flow ionized air moves from electrode to ground in order to induce the shear flow, so-called Corona wind, it is secondary flow.

Many researchers have contributed to the development of EHD and its implementation in the following four main groups of applications: increasing flow, spread flow, induced flow, and mixing processes, respectively. For increasing flow, pumping is often cited as a general application which requires ongoing development of microfabricated motors and other actuators. A practical requirement for EHD pumping is the induction of free electric charge in the volume of the fluid to be pumped or on its interface with another material.[5–7] For spread flow, electrospraying is a method of liquid atomization by electrical forces. Droplets produced by electrospraying are charged which prevents their coagulation and promotes self-dispersion. Electrospraying is applied in microfluidic devices and nanotechnology for microencapsulation, fine powder production, or thin film deposition.[8–12] For induced flow, electrostatic precipitation has a very complex interaction between the electric field, gas, and particulate flow. The motion and precipitation of dust particles in electrostatic precipitation depends on the electric field, space charge, gas flow field, and dust particle properties.[13–15] For mixing processes, studies demonstrating the enhancement of heat transfer and mass transport, especially with respect to evaporators and condensers, has been performed.[16–19] The rapid control of performance by varying the applied electric field, the simple design, and low power requirements are all advantages of the application of EHD. As shown in previous studies, the mixing process application of EHD has been performed by researchers around the world.

Many researchers are focused on mixing applications such as drying processes, convective heat transfer, and heat exchangers. Fernandez and Poulter[20] experimentally presented an electrohydrodynamically enhanced oil heater having annular cross-section. The result showed that when an electric field was applied across the annular gap, it induced a very strong radial motion of the fluid resulting in heat transfer increases of more than 20 times over the fully developed laminar flow. Wang and colleagues[21] experimentally analyzed the natural convection heat transfer with an applied uniform electric field. This correlation was applicable over a range of electric Rayleigh numbers from 3×10^4 to 4×10^7 and heat fluxes from 0.5 kW/m^2 to 3.5 kW/m^2. This correlation is suitable only for the liquid ether in some range of heat fluxes. Lai and Wang[22] experimentally evaluated the enhancement of water evaporation from partially wetted glass beads by corona wind. The results showed that the electric field was effective in the enhancement of water evaporation from partially wetted glass beads, but its effectiveness diminished when the water level in the glass beads receded. By applying auxiliary heating, this shortcoming of EHD-enhanced drying could be overcome. Kasayapanand and Kiatsiriroat[23] numerically investigated the electric field effect on natural convection in partially open square cavities with thin fins. It was found that the flow and heat transfer enhancements decreased as a function of the Rayleigh number. The volume flow rate and heat transfer coefficient were substantially improved by EHD especially at low aperture size, high aperture position, and high inclination angle. The maximum convective heat transfer was obtained at the minimum electrical energy consumption by placing electrodes at a suitable position.

From previous studies, Saneewong Na Ayuttaya and colleagues[5] were early investigators of swirling flow in 2012. In this study, shear flow was established to appear due to differences in fluid velocity between charged airflow and uncharged airflow. The characteristic and direction of flow pattern are induced from electric forces. This causes shear flow to become the swirling flow. Furthermore, EHD technique can be utilized for controlling the patterns of airflow. In order to enhance convective heat transfer above a sample surface, the thermal boundary layer from the material surface is eliminated.

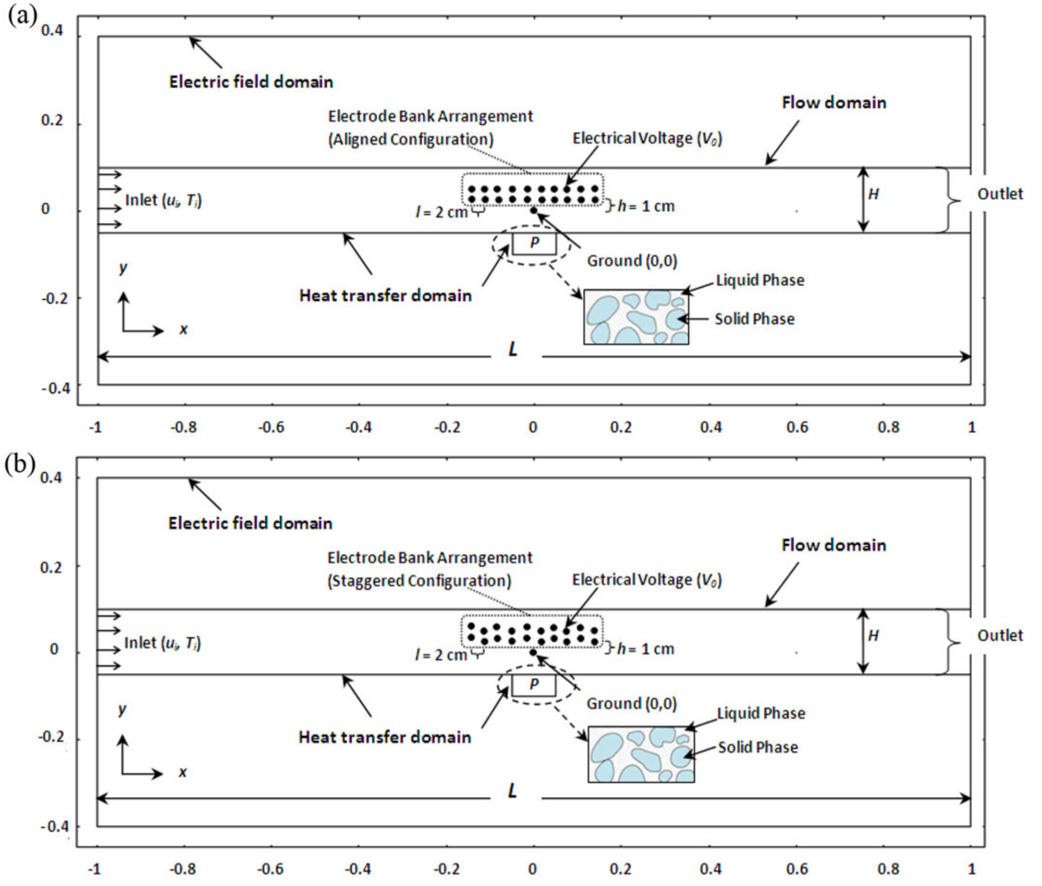

FIGURE 1 A schematic view of the main computational domain and geometric parameters (a) aligned configuration and (b) staggered configuration [Color figure can be viewed at wileyonlinelibrary.com]

Afterwards, the heat transfer within the sample is increased. Recently, our research group has tried to numerically investigate the EHD force for heat transfer enhancement. Due to the complexity of the problem, a conjugate approach is studied for enhancing heat transfer in a sample. Based on the literature review of the conjugate approach,[24–27] the conjugate problem addresses the thermal interaction between a body and a fluid flowing over or through it. In the present study, the characteristics of electric field, swirling flow, and temperature distribution from electrode arrangements, that is, aligned and staggered configuration in channel flow subjected to EHD, for enhancing fluid flow and heat transfer within a porous medium are systematically investigated. In addition, inlet velocity ($u_i = 0.1$ m/s (Re = 852)) is compared with no inlet velocity ($u_i = 0$ m/s (Re = 0)). Finally, number of electrodes (n) and rows of electrodes are varied from 1 to 40 and 1 to 4, respectively.

2 | GOVERNING EQUATION

The configuration under investigation in the present study consists in a channel flow where air enters at a given velocity (u_i) and temperature (T_i). Fig. 1 shows a schematic view of three main computational domain and geometric parameters. The first, second, and third domains are electric field, flow, and heat transfer, respectively. For the first, dimensions of the electric field domain are 2.0 m long (L) × 0.8 m high (H). The second and the third domains, the dimensions of flow and heat transfer domains are 2.0 m long (L) × 0.15 m high (H). It can be seen that the electric field domain is larger than flow and heat transfer domains. This is because the electric field is treated as continuous on the channel wall. Also, the electrode or multiple electrodes and ground are assumed to be a circle with a diameter of 0.5 mm. The gap of each electrode in the horizontal (l) and vertical (h) directions are 2 cm and 1 cm, while the position of the ground is always fixed at $x = 0$ m and $y = 0$ m. For electrode bank arrangements, the aligned configuration (Fig. 1a) and staggered configuration (Fig. 1b) are compared. A porous medium block (P) of 10 cm × 5 cm is placed at the lower wall and the top surface is exposed to hot airflow.

2.1 | Electric field equation

As the airflow is appeared by the Coulomb force acting on the space charge density (q), the corona discharge occurs only in the vicinity around the electrode wire, the dielectric properties are constant, and the effect of magnetic field is negligible. The electric problem is then governed by Maxwell's equations of EHD (Eqs. (1) to (3)) and Ohm's law (Eq. (4)).

$$\vec{E} = -\nabla V, \tag{1}$$

$$\nabla \cdot E = {}^{q}\!/_{\varepsilon}, \tag{2}$$

$$\nabla \cdot \vec{J} + \frac{\partial q}{\partial t} = 0, \tag{3}$$

$$\vec{J} = qb\vec{E} + q\vec{u}, \tag{4}$$

where E and J are electric field and current density, respectively. The electric force per unit volume ($\vec{f}_E$) is the main driving force of corona-induced flow mixing. It is expressed as[28]:

$$\vec{f}_E = q\vec{E} - \frac{1}{2}\vec{E}^2\nabla\varepsilon + \frac{1}{2}\nabla\left[\vec{E}^2\left[\frac{\partial\varepsilon}{\partial\rho}\right]_T\rho\right]. \tag{5}$$

For corona discharge to appear at room temperature and atmospheric pressure conditions, dielectric permittivity (ε) can be assumed to be constant. Therefore, the second and third terms on the right-hand side of Eq. (5) are negligible.[5]

2.2 | Flow field equation

The flow field is unsteady, single phase, and incompressible flow. The fluid physical properties are assumed to be constant. The continuity equation (Eq. (6)) and Navier–Stokes equation (Eq. (7)) which coupled with the Coulomb force equation can be written in the following form:

$$\nabla \cdot \vec{u} = 0, \tag{6}$$

$$\rho\left[\frac{\partial\vec{u}}{\partial t} + (\vec{u}\cdot\nabla)\vec{u}\right] = -\nabla\vec{P} + \mu\nabla^2\vec{u} + q\vec{E}. \tag{7}$$

2.3 | Heat transfer equation

Within a channel flow, the thermophysical properties are taken to be constant. The effect of buoyancy is negligible, no emission or absorption of radiant energy. Temperature distribution is calculated by the energy equation (Eq. (8)):

$$\rho C_p \left[\frac{\partial T}{\partial t} + \vec{u}\nabla T\right] = k\left(\nabla^2 T\right), \tag{8}$$

where C_P is the specific heat and k is thermal conductivity. Within a porous medium, the governing equations describing the heat transfer within the porous sample is calculated from Eqs. (9) and (10) and effective thermal conductivity (k_{eff}) in a porous medium is computed by Eq. (11).[29] A porous medium is a material containing voids and it is most often characterized by its porosity. The permeability of the medium can sometimes be derived from the respective properties of its constituents (solid matrix and fluid) and the pore space accessible to flow but such a derivation is usually complex. So Brinkmann model is used for the effect of porous medium:

$$\frac{1}{\phi}\frac{\partial \vec{u}}{\partial t} + \frac{1}{\phi^2}(\vec{u}\cdot\nabla)\vec{u} = -\frac{1}{\rho_l}\nabla P + \frac{\mu}{\rho\phi}\nabla^2\vec{u} - \frac{\mu\vec{u}}{\rho\kappa}, \tag{9}$$

$$(\rho C_p)_{eff}\frac{\partial T}{\partial t} = (\rho C_p)_l \vec{u}\nabla T = k_{eff}\nabla^2 T, \tag{10}$$

where ϕ is porosity and κ is permeability in a porous sample is computed from

$$k_{eff} = (1-\phi)\kappa_s + \phi\,\kappa_l, \tag{11}$$

and

$$(\rho \mathrm{C_p})_{\text{eff}} = (1-\phi)(\rho C_p)_{\text{s}} + \phi\,(\rho \mathrm{C_p})_{\text{l}}. \tag{12}$$

In order to investigate the convective heat transfer coefficient (h_c) (Eq. (13)) and the augmented heat transfer (Nu) (Eq. (14)) on the porous sample surface, the porous medium material is placed under the bottom wall of channel flow and only the upper surface of it exposed to hot airflow. So the convective heat transfer is defined by the thermal equilibrium:

$$h_c = -\frac{k}{\Delta T}\frac{\partial T}{\partial n}, \tag{13}$$

$$Nu = \frac{h_c L}{k}. \tag{14}$$

3 | BOUNDARY CONDITIONS

The boundary condition of this problem is shown in Fig. 2. The computational scheme is assembled in a finite element model using a collocation method.[30] Lagrange quadratic element is chosen as the basic function with triangular shapes. The convergence curve resulting from the convergence test is grid validation between percent error of electric field and different elements from simulation. With percentage

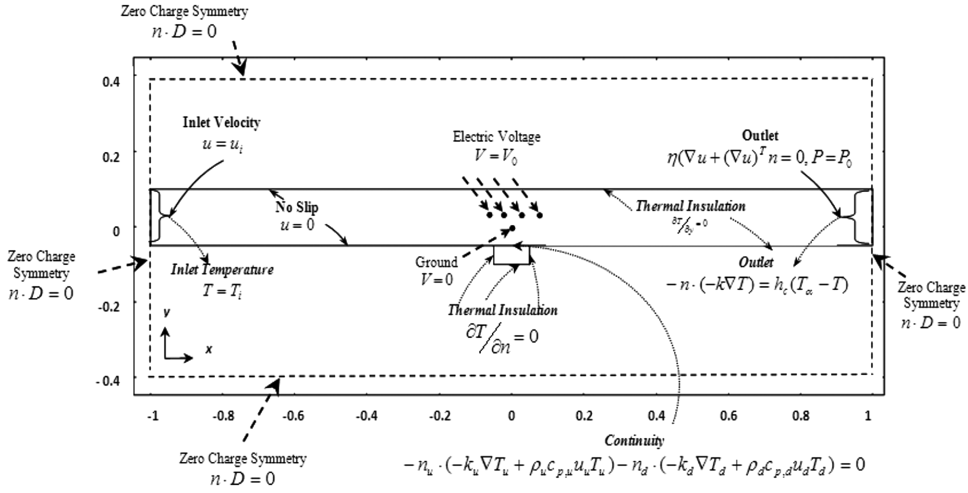

FIGURE 2 Boundary conditions of electric field, flow field, and temperature field used in analysis

error of temperature lower than 0.1, this convergence test leads to a mesh having approximately 7000 elements.

3.1 | Electric field boundary condition

The outer sides of the electric field boundary conditions are shown in Eq. (15) which considered as zero charge symmetry. Electrode and ground are considered as electrical voltage ($V = V_0$) and ground ($V = 0$) boundary condition, respectively:

$$n \cdot D = 0. \tag{15}$$

3.2 | Flow field boundary condition

The inlet velocity is assumed to be uniform. The pressure at the outlet boundary condition is considered with no viscous stress, as shown in Eq. (16). Therefore, this boundary condition specifies vanishing viscous stress along with a Dirichlet condition on the pressure:

$$\eta(\nabla\vec{u} + (\nabla\vec{u})^T \cdot n = 0 \,\text{and}\, \vec{P} = \vec{P}_0. \tag{16}$$

The upper and lower of channel flow are considered as no slip boundary conditions, $u_{\text{wall}} = 0$.

3.3 | Temperature boundary condition

Within the channel flow, the inlet temperature, $T_i = 60\,^{\circ}\text{C}$, and the boundary condition at the outlet are shown in Eq. (17). The upper and lower walls of channel are insulated, as shown in Eq. (18). The condition prescribes:

$$-n \cdot (-k\nabla T) = h_c(T_\alpha - T), \tag{17}$$

$$\frac{\partial T}{\partial y} = 0. \tag{18}$$

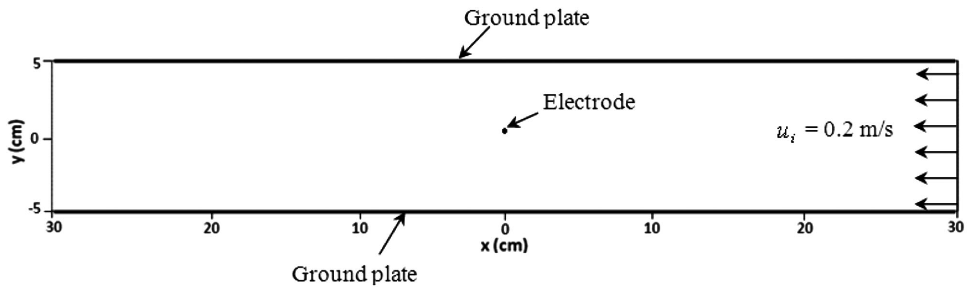

FIGURE 3 Geometry of the validation model obtained from Chun and colleagues[31]

The porous sample is placed under the bottom wall of channel flow, and only the upper surface of it is exposed to hot airflow. The other surface is considered as an insulated boundary condition (Eq. (19)):

$$\frac{\partial T}{\partial n} = 0, \tag{19}$$

where n coordinate in x and y axis. The uniform initial temperature of porous sample ($T_s(t_0)$) is 20 °C. At the interface of hot airflow and sample, it is evident that a generalized conjugate approach to the combined fluid flow and heat transfer process, the interface of hot airflow and sample is solved by using Eq. (20). It is defined as:

$$-n_u \cdot (-k_u \nabla T_u + \rho_u C_{p,u} \vec{u}_u T_u) - n_d \cdot (-k_d \nabla T_d) = 0. \tag{20}$$

The upper and the lower interfaces are designated by subscript u and d, respectively.

4 | MODEL VERIFICATION

To verify the accuracy of flow patterns, the resulting data is validated against numerical results previously reported by Chun and colleagues.[31] Fig. 3 shows geometry of two-part domain, and the first and second parts are electric field and flow domains, respectively. In the validation, a two-dimensional (2D) model has been investigated. Dimensions of domain are 60 cm long × 10 cm high. Electrode wire is assumed to be a circle, it is always fixed at $x = 0$ m and $y = 0$ m, and ground plates are installed in both upper and lower walls. Air flows from right to left direction, and inlet velocity (u_i) is 0.2 m/s (Re = 1333). Comparison of flow patterns with and without EHD is shown in Fig. 4. Without EHD ($V_0 = 0$ kV), Fig. 4(a) shows test results of Chun and colleagues,[31] and Fig. 4(b) shows present simulation. It can be seen that the airflow in both cases move outwardly from right to left direction, and airflow avoids the electrode wire. In fact, the electrode wire is specified for no slip boundary conditions. Comparison between Chun and colleagues[31] Fig. 4(c) and the present simulation Fig. 4(d) are also shown with EHD ($V_0 = 19.9$ kV). Swirling flow is observed, and small double cells appear near the upper and lower walls. Small double cells of swirling flow between electrode and ground are induced by shear flow. Furthermore, the small cell at the upper and lower wall appears in the clockwise and the counterclockwise directions, respectively. The small double cells are presented near the ground plate or close to the upper and lower wall.

In order to confirm the accuracy of the present numerical model, flow visualization from the experimental set up is generated using the incense smoke technique. The hot airflow is supplied from a blower

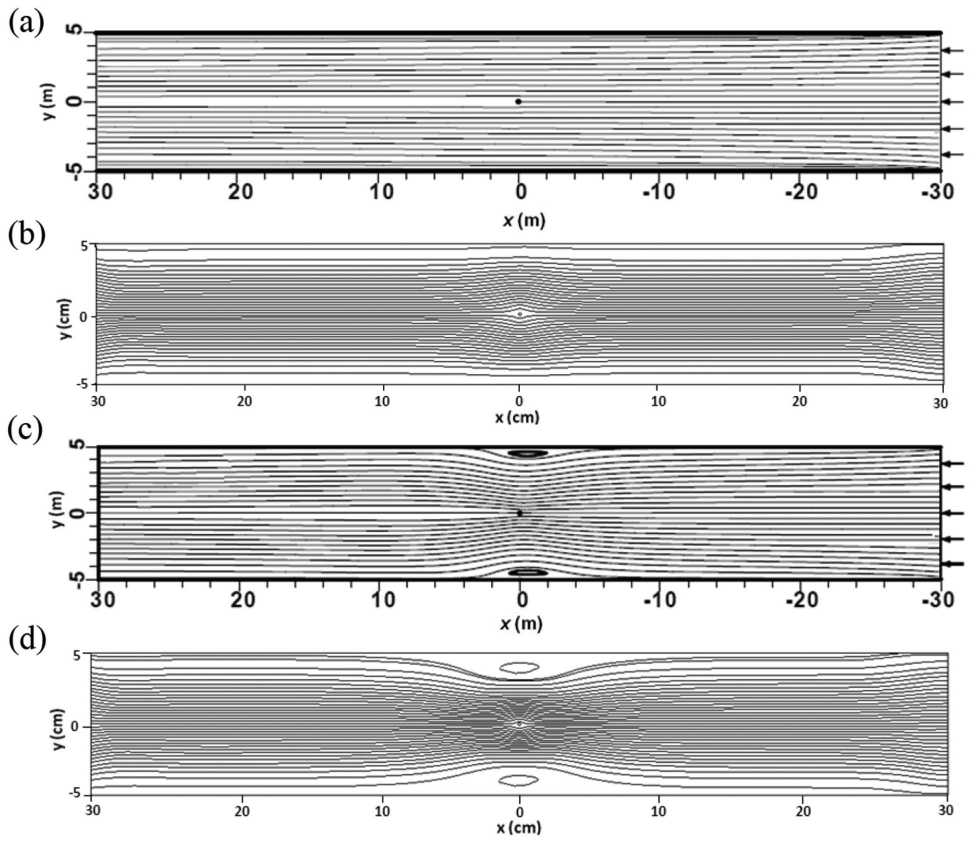

FIGURE 4 Test results for validation purposes when $u_i = 0.2$ m/s: (a) Chun and colleagues (2007) when $V_0 = 0$ kV, (b) present simulation when $V_0 = 0$ kV, (c) Chun and colleagues (2007) when $V_0 = 19.9$ kV, and (d) present simulation when $V_0 = 19.9$ kV

and electric heater. A high voltage power supply (ACOPIAN model: NO30HP2M.-230) is used to create electrical voltage. A copper electrode wire is suspended from the top of rectangular duct and is placed in the front of packed bed, and a copper ground is suspended horizontally across the test section. In order to observe the motion of airflow subjected to the electric field, the incense smoke technique is used by means of a smoke generator (GUNT HAMBURG: HM 170.52). A spotlight of 500 W is placed at the outlet of the rectangular duct flow with the direction of light opposite to flow. In the experimental set up, the distance between the electrode and ground in the vertical direction and the horizontal direction are fixed at 2 cm and 0 cm, respectively, and the inlet airflow is zero ($u_i = 0$ m/s). The numerical results are then compared to the experimental results of airflow motion, as shown in Fig. 5. The present simulated result is solved by the finite element method using the collocation method, and the boundary conditions of numerical modeling are showed in Fig. 2. For without electric field (no EHD), swirling flow cannot be observed, and airflow velocity is zero. This is because primary flow or external force is not formed in the rectangular duct. Fig. 5 shows the validation results of the airflow motion under the electric field ($V_0 = 10$ kV). Figs. 5(a) and (b) are the experimental and present simulation results, respectively. It is observed that the double cells of swirling flow with symmetrical patterns are clearly displayed at the location close to the electrodes and ground. This is because the absence of inlet airflow causes no external force disturbing the purely corona wind for this case. Double cells of swirling flow between the electrodes and ground are induced by shear flow due to the difference between charged

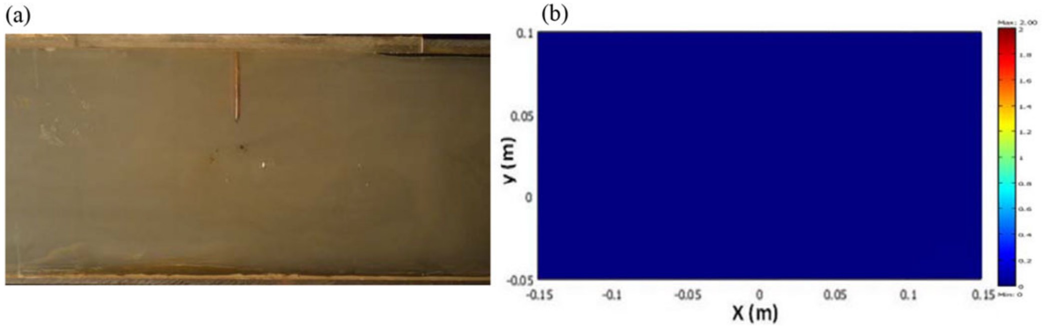

FIGURE 5 The validation results of the airflow motion in case of without electric field (No EHD) and absence of inlet airflow (u_i = 0 m/s): (a) Experimental result and (b) Present simulation result. [Color figure can be viewed at wileyonlinelibrary.com]

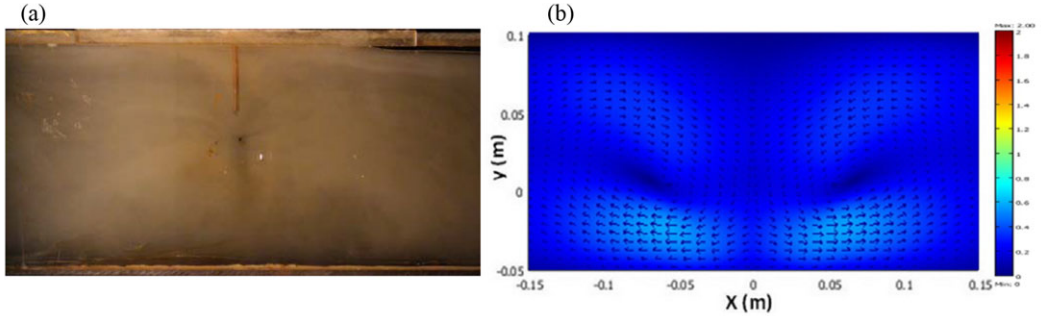

FIGURE 6 The validation results of the airflow motion under electric field (V_0 = 10 kV) and absence of inlet airflow (u_i = 0 m/s): (a) Experimental result and (b) present simulation result [Color figure can be viewed at wileyonlinelibrary.com]

and uncharged airflow velocities. The charged and uncharged airflow velocities lead to primary and secondary flow, respectively. Furthermore, the front cell and latter cell appear in clockwise and counterclockwise directions, respectively, and swirling flow can induce airflow velocity.

From the experimental result (Fig. 6), the wind tunnel is mostly made of acrylic plate. The tunnel is 4.5 m long with a dimension of 15 × 15 cm^2. Each tunnel is connected with a screw bolt and an insulator in between to protect the air from leaking. The tunnel is design to supply hot airflow with a full developed profile and the purpose of straightener is to adjust the airflow flow. Straightener will smooth and force the air to flow in straight line by using a small hollow pipe. A blower is used to supply the air to the wind tunnel. The amount of air supply can be control by adjusting the lid that covers the suction area. Incense smoke technique is used for flow visualization and the motion of flow is continuously captured by digital video camera recordings, inlet airflow moves from the left to the right direction (u_i = 0.35 m/s). A copper electrode wire and ground wire are suspended from the top wall and horizontally across the test section, respectively. The tip of the electrode and ground are covered with the corona current. A solid material of rigid body is installed within the rectangular duct. The simulation results (Figs. 7 and 8) are assembled in the finite element model using a collocation method. When electric field boundary condition is used, the outer sides are considered as zero charge symmetry, as shown in Eq. (15). The electrical voltage ($V = V_0$) is fixed at the tip of electrode and the ground is $V = 0$. When flow field boundary condition is used, the inlet velocity is assumed to be uniform and the outlet is considered with no viscous stress, as shown in Eq. (16). The upper and lower of channel

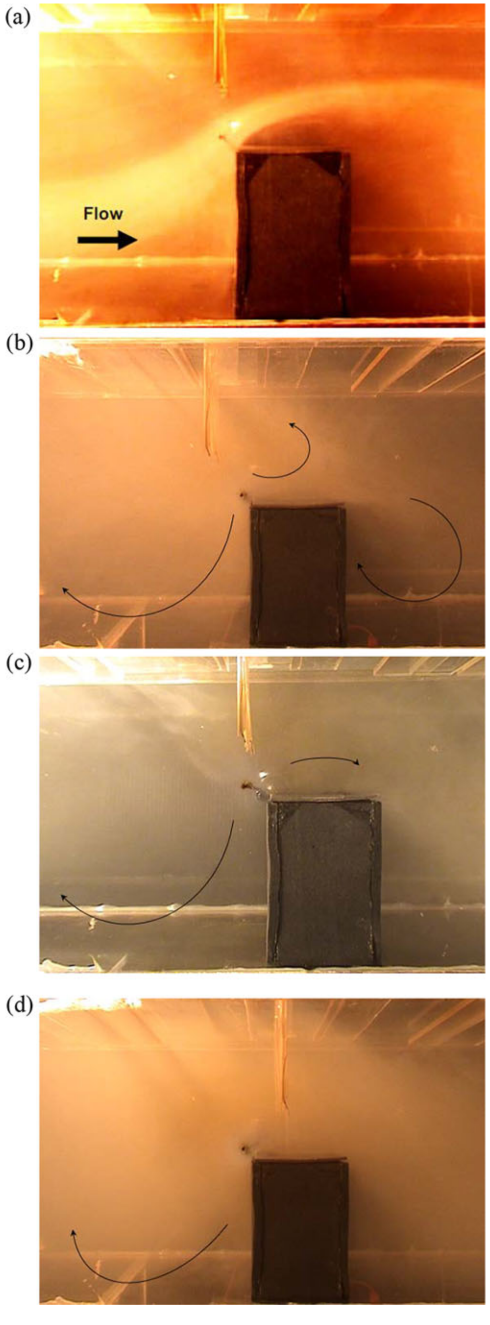

FIGURE 7 The experimental flow visualization when u_i = 0.35 m/s: (a) No EHD, (b) l = –4 cm and V_0 = 15 kV, (c) l = 0 cm and V_0 = 15 kV, and (d) l = 4 cm and V_0 = 15 kV [Color figure can be viewed at wileyonlinelibrary.com]

flow are considered as no slip boundary conditions (u_{wall} = 0) and no slip boundary conditions are considered all of sample surfaces. From Figs. 7(a) and 8(a), the primary flow or inlet airflow is moved from left to right direction but avoids the solid black block so that a separation zone appears above the solid black block. When electrical voltage is applied (V_0 = 15 kV), l = –4 cm, l = 0 cm, and l = 4 cm are showed in Figs. 7(b) to 8(b), Fig. 7(c) to 8(c), and Fig. 7(d) to 8(d), respectively. From Figs. 7(b) to 8(b),

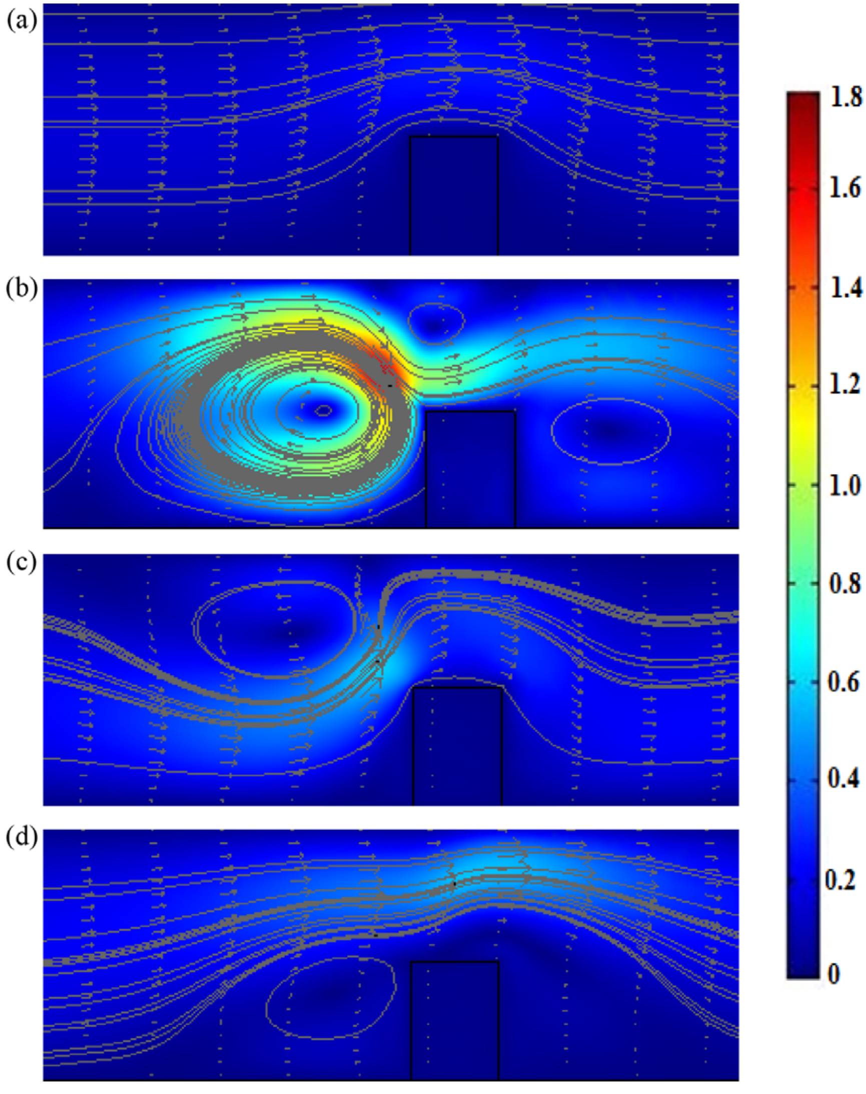

FIGURE 8 The simulation result when $u_i = 0.35$ m/s: (a) $V_0 = 0$ kV, (b) $l = -4$ cm and $V_0 = 15$ kV, (c) $l = 0$ cm and $V_0 = 15$ kV, and (d) $l = 4$ cm and $V_0 = 15$ kV [Color figure can be viewed at wileyonlinelibrary.com]

two cells of swirling flow or secondary flow with asymmetrical patterns appear in the case with electric fields and the front cell and latter cell appear in clockwise and counterclockwise, respectively. It can be seen that the front cell is bigger than the latter cell, because the front cell is supported in the primary flow direction, but the latter cell appears above the solid black block as the electric field effect can include drag reduction from the ion wind associated with atmospheric corona discharges. In addition, the clockwise direction of fluid flow is swirled behind the solid black block, because it is affected by the latter cell and solid black block. Figs. 7(c) and 8(c) show the one big cell in the clockwise direction, and fluid flow is moved above the solid black block, as the electrode arrangement is not supported by the primary flow direction making the swirling flow less concentrated. Figs. 7(d) and 8(d) show the one big cell in the clockwise direction, but swirling flow is not clearly observed because the shear flow direction is not supported by the primary flow direction. The comparison test results of both techniques are shown to be in good agreement confirming the accuracy of the present simulation result. Furthermore, flow

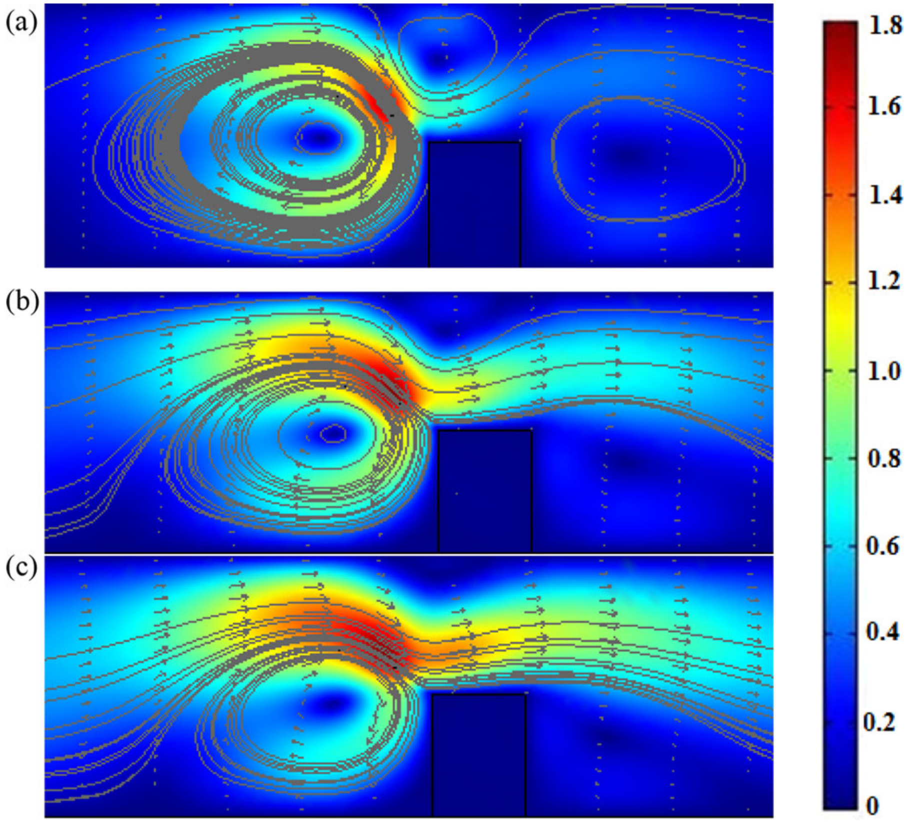

FIGURE 9 The simulation result when V_0 = 15 kV and l = –4 cm: (a) u_i = 0.2 m/s, (b) u_i = 0.6 m/s, and (c) u_i = 1 m/s [Color figure can be viewed at wileyonlinelibrary.com]

visualization from simulation appears more clearly than from the incense smoke technique because very short time exposure pictures of swirling flow were captured. The simulation result with various inlet velocities (u_i) when $V_0 = 15$ kV and $l = -4$ cm is shown in Fig. 9. From Fig. 9(a), two cells of swirling flow and one cell of fluid flow are clearly shown within channel flow. The big front cell and the small latter cell of swirling flows appear in the clockwise and counterclockwise directions, respectively. The front cell of swirling flow from Fig. 9(c) is smaller than the front cell of swirling flow from Fig. 9(b). It can be seen that the size of front cell decreases with increase inlet velocity. The maximum velocity (u_{max}) increases with increasing inlet velocity, but the maximum velocity ratio (u_{max}/u_i) significantly decreases with increasing inlet velocity or $u_{max}/u_i = 1.7255u_i^{-0.941}$, as shown in Fig. 10. This is because the inlet velocity of air is increased; the strength of swirling flow is decreased because inertial force is greater than the electric force. It means the Reynolds number is small so the effect of electric force is dominant.[5]

5 | RESULTS AND DISCUSSION

Subdomain modeling parameter values are used for the entire simulation space which comprised the inside channel flow, where classical properties are shown in Table 1 and thermal properties are shown in Table 2. They are solved using models reported by Saneewong Na Ayuttaya and colleagues[5] and

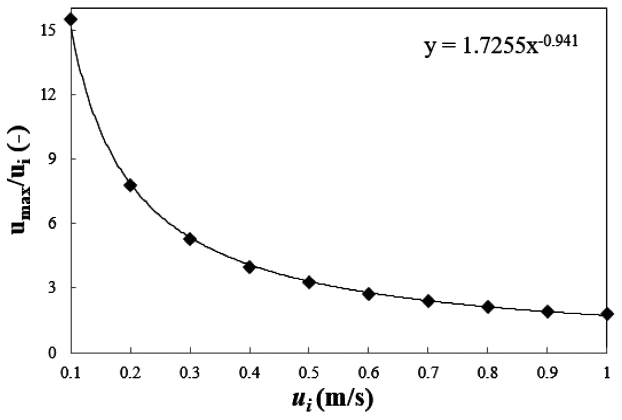

FIGURE 10 Maximum velocity ratio in various inlet velocity when $V_0 = 15$ kV

TABLE 1 Classical properties

Modeling parameter	b (m^2/V.s)	ε (F/m)	ϕ	κ (m^2)	Saturation
Hot-airflow	1.80×10^{-4}	8.85×10^{-12}	–	–	–
Water	–	–	–	–	1
Solid	–	–	0.371	3.52×10^{-11}	–

TABLE 2 Thermal properties

Modeling parameter	ρ (kg/m^3)	η (m^2/s)	K (W/m.K)	C_p (kJ/kg.K)
Hot-airflow	1.060	1.76×10^{-5}	0.028	1.008
Water	998	1.005×10^{-5}	0.588	4.186
Solid	2500	–	0.14	0.8

Source of hot-airflow: Saneewong Na Ayuttaya S, Chaktranond C, Rattanadecho P & Kreewatcharin T (2012) Effect of Ground Arrangements on Swirling Flow in a Channel Subjected to Electrohydrodynamic Effects. ASME J. of Fluids Eng 134: 051211-9.
Source of water sample and porous sample (water and solid): Sungsoontorn S, Rattanadecho P & Pakdee W (2011) One-Dimensional Model of Heat and Mass Transports and Pressure Built -Up in Unsaturated Porous Materials Subjected to Microwave Energy. Drying Technol 29: 189-204.

Sungsoontorn and colleagues.[32] In order to study the electric field influence of the flow structure, the gap in the horizontal and vertical directions are fixed at $l = 0$ cm and $h = 2$ cm, respectively. The inlet velocity is zero ($u_i = 0$ m/s), and the electrical voltage is controlled at $V_0 = 10$ kV. Fig. 11 shows electric field distributions and swirling flow under the electric field in the x-y plane which focus on the plane of the electrode and ground. Fig. 11(a) describes the electric field moving outwardly from the electrode to ground concentrating at both electrode and ground area. The electric field effect is induced by shear flow and swirling flow under electric field, or secondary flow is induced from primary flow, as shown in Fig. 11(b). Focusing on the shear flow effect, the big double cells of swirling flow with symmetrical patterns are clearly displayed at the location close to the electrodes and ground area. These cells appear at the upper wall area, while the front cell and latter cell appear in clockwise and counterclockwise directions, respectively. On the other hand, the small double cells of swirling flow are induced from the big double cells of swirling flow and appear at the lower wall area, while the front cell and latter cell appear in counterclockwise and clockwise directions, respectively. In the absence of inlet velocity (no external force), the shear flow effect (or pure corona wind) increases the magnitude of the swirling flow.

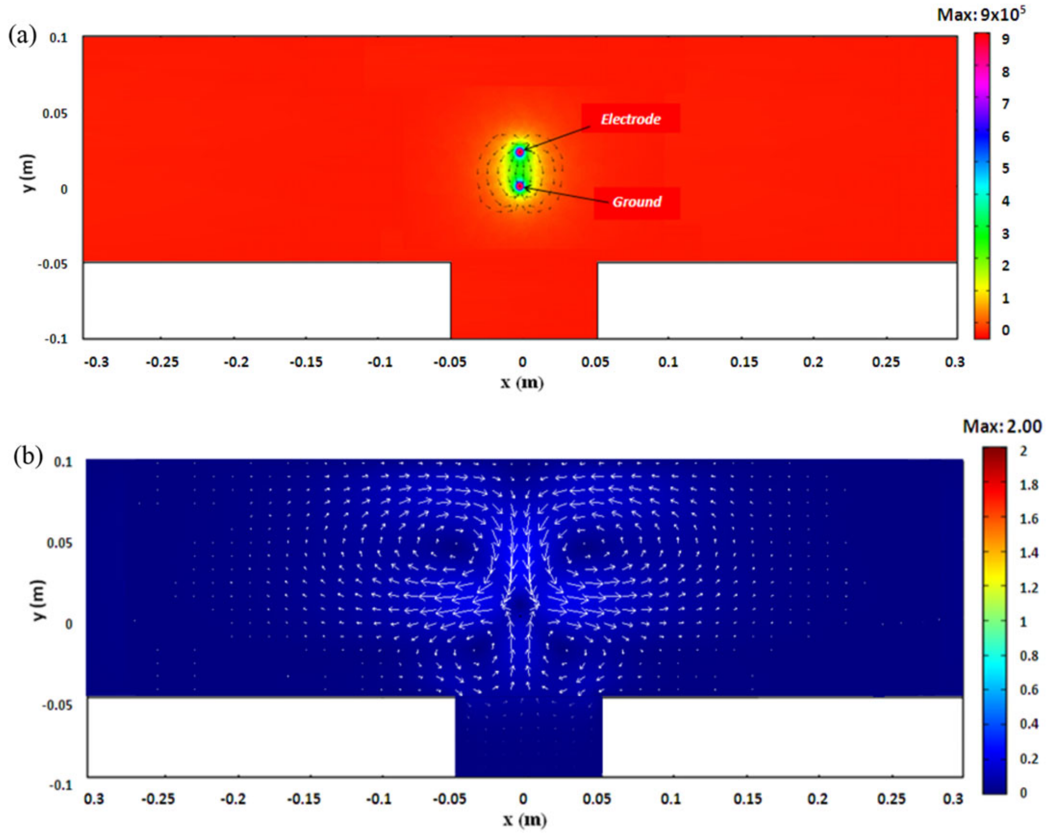

FIGURE 11 Effect of electric field on flow structure in x–y plane when u_i = 0 m/s, l = 0 cm, h = 2 cm, and V_0 = 10 kV. (a) Electric field distribution and (b) swirling flow under electric field [Color figure can be viewed at wileyonlinelibrary.com]

The configuration of the electrode bank is affected by electric field patterns. Figs. 12 and 13 show aligned and staggered electrode configurations, respectively. The number of electrodes per row is fixed at n = 10 and V_0 = 20 kV. Single row (n = 10), double rows (n = 20), triple rows (n = 30), and quadruple rows (n = 40) are compared. The electric field moves outwardly from electrode to ground and it is concentrated at both electrode and ground area. Furthermore, electric field is more expanded with increasing number of electrodes, and the strength of shear flow is increased with electrode number increasing. The electric field pattern of staggered configuration is more complicated than the aligned configuration. By increasing the number of electrodes and rows, the electric field pattern is clearly more complicated. This is because the electric field (E) from Eq. (1) depends on electrical voltage (V_0) so electric field intensity increases with increasing number of electrodes.[5] Furthermore, electric field is independent of inlet velocity and time.

The swirling flow from shear flow effect is induced by the electric field, and the swirling flow in a channel can induce fluid flow within a porous medium. At n = 10 and V_0 = 20 kV, in case without inlet velocity (u_i = 0 m/s (Re = 0)) and with inlet velocity (u_i = 0.1 m/s (Re = 852)) are shown in Figs. 14 and 15, respectively. From previous studies,[33] the inertial force (inlet velocity) is superior to the Coulomb force (electric force) when inlet velocity is increased. The laminar flow is the suitable for EHD mechanism, so comparison between 0 m/s (Re = 0) and 0.1 m/s (Re = 852) of inlet velocity are investigated. Therefore, the swirling flow appears with no external force or the absence of inlet

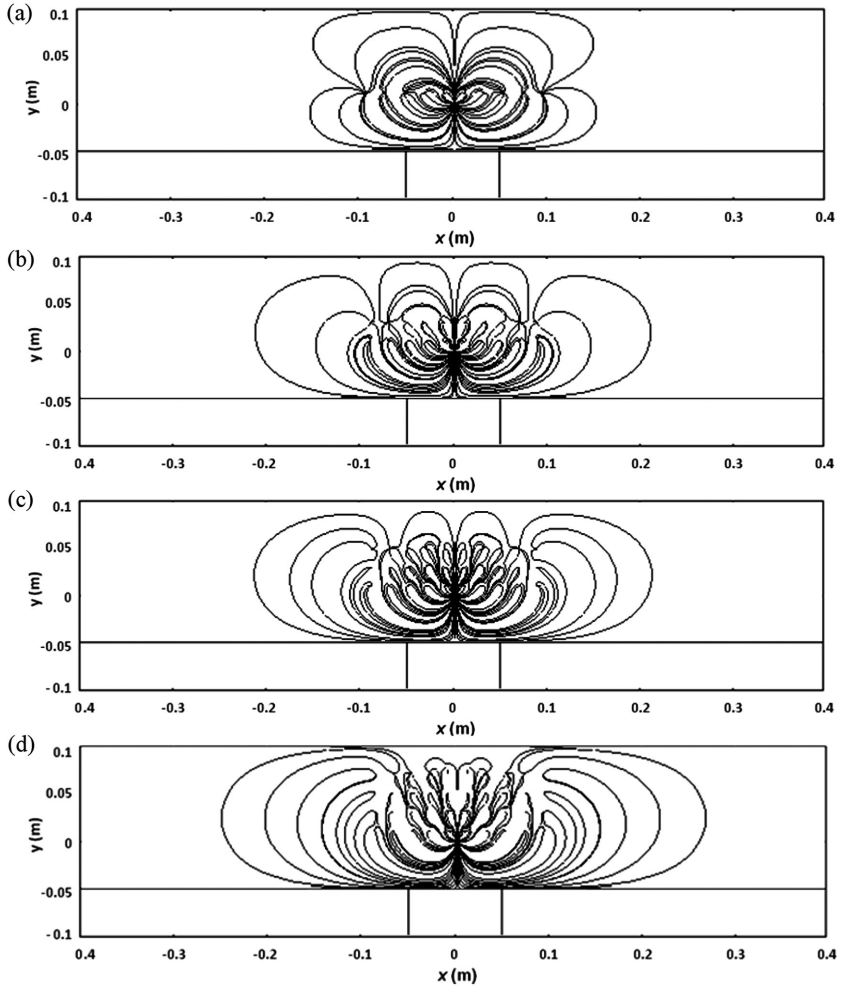

FIGURE 12 Electric field in various row and n of aligned configuration: (a) single row ($n = 10$), (b) double rows ($n = 20$), (c) triple rows ($n = 30$), and (d) quadruple rows ($n = 40$) when $V_0 = 20$ kV

velocity ($u_i = 0$ m/s), as shown in Fig. 14. For aligned electrode configurations Figs. 14(a) and (b), two big cells of swirling flow is observed, and the front and the latter cells are swirled in the counter-clockwise and clockwise directions, respectively. For staggered configuration Figs. 14(c) and (d), the two big cells and the two small cells of swirling flow appear, and the front and the latter of the big cells are swirled in the counterclockwise and clockwise directions, respectively. They slice the air so that the small two cells appear. This is because electric field patterns from staggered configurations (Fig. 13) are more complicated than from aligned electrode configurations (Fig. 12). In the case of external force or inlet velocity ($u_i = 0.1$ m/s), the air flows from the left to the right direction and it is swirled when it moves in the electrode and ground zone. Swirling flow appears in the counterclockwise direction, and the maximum velocity is clearly displayed at the location closest to the lower wall, as shown in Fig. 15. In addition, the swirling flow from triple rows Figs. 14(b), 14(d), 15(b), and 15(d) of electrodes are spread wider than swirling flow from single rows Figs. 14(a), 14(c), 15(a), and 15(c). This is because increasing the number of electrodes increases the shear flow effect. The Coulomb force or electric force depends on electrical voltage (V_0); it leads to changes in the direction of flow patterns.

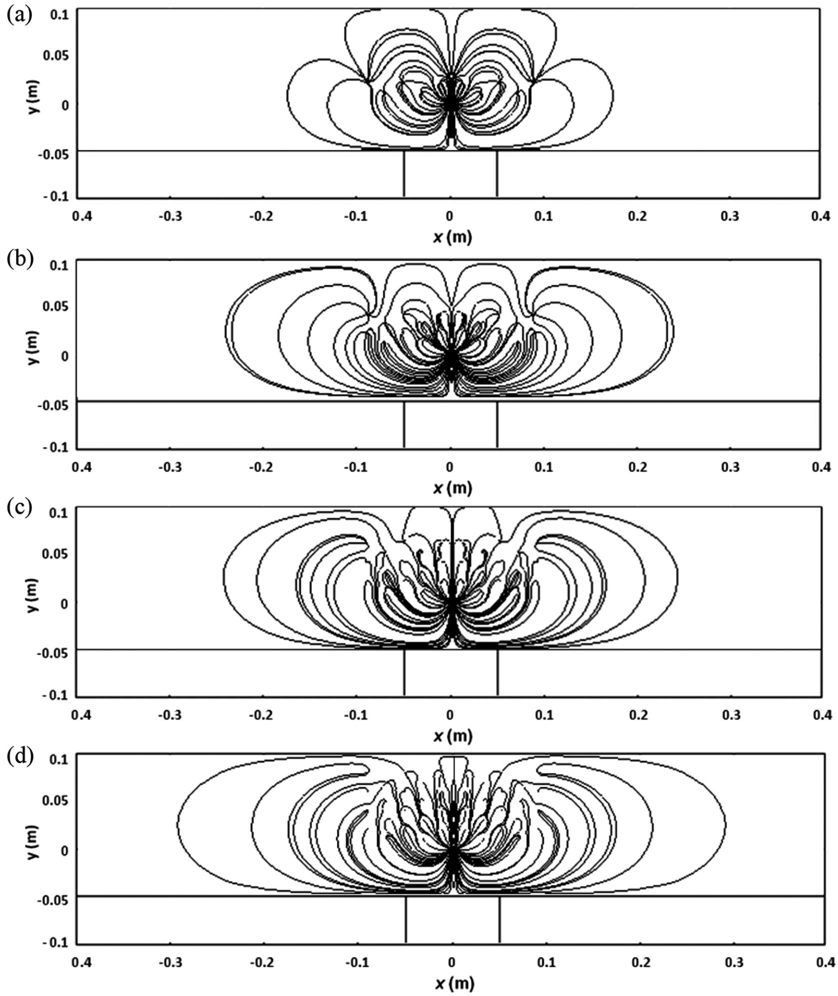

FIGURE 13 Electric field in various row and n of staggered configuration: (a) single row and $n = 10$, (b) double rows and $n = 20$, (c) triple rows and $n = 30$, and (d) quadruple rows and $n =$ when $V_0 = 20$ kV

Implementing higher electrical voltage significantly increases the current passing through the ground wire which makes the effect of corona wind greater in comparison with lower voltages. The swirling flow zone of staggered configuration is expanded more than the aligned configuration, but swirling flow from aligned configuration is more turbulent. Furthermore, the fluid flow within the porous medium is affected by the swirling flow in a channel. The fluid flow pattern and fluid flow direction within the porous medium have the same trend with swirling flow in a channel, but swirling flow and fluid flow are independent over time. Nevertheless, the strength of swirling flow is decreased when inlet velocity is increased, whereas the inlet velocity from $u_i = 0.1$ m/s supports the strength of the electric field. Therefore, as a function of the EHD mechanism, the electric field and flow field are determined by more than only the electric field or the absence inlet velocity ($u_i = 0$ m/s).

As addressed above, swirling flow patterns depend on electrode bank arrangements and the number of electrodes. In order to study temperature distribution (isotherm line) in channel flow and within porous medium, the number of electrodes per row is fixed at $n = 10$ and $V_0 = 20$ kV. Temperature in channel flow and within the porous medium is 60 °C and 20 °C, respectively. The conjugate approach

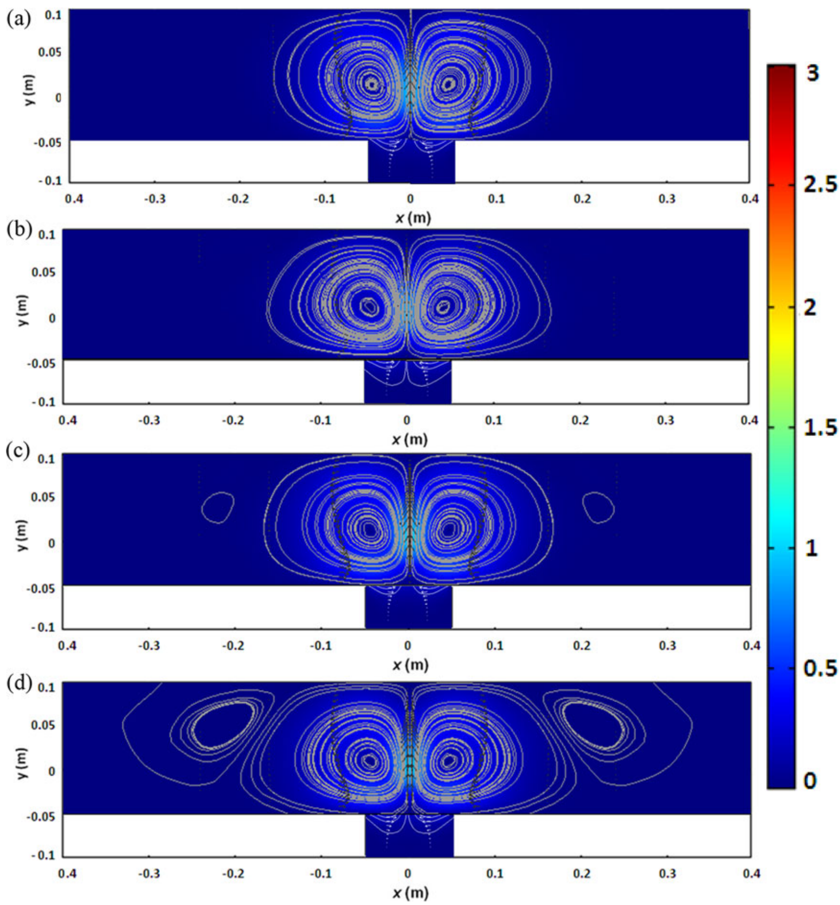

FIGURE 14 Swirling flow (m/s) in a channel flow and fluid flow within porous medium in various rows and n: (a) single row ($n = 10$) of aligned configuration, (b) triple rows ($n = 30$) of aligned configuration, (c) single row ($n = 10$) of staggered configuration, and (d) triple rows ($n = 30$) of staggered configuration when $V_0 = 20$ kV and $u_i = 0$ m/s [Color figure can be viewed at wileyonlinelibrary.com]

describes heat transfer between a body and fluid flowing over or inside it as a result of interactions between two objects. From the swirling flow effect in the channel, fluid flow above the sample surface is faster causing greater heat transfer into the porous medium. This causes the temperature of the sample is more rapidly increased. When time progress, the heating zone in channel flow passes through the interface of hot airflow and the porous medium, after which temperature within the porous medium is increased. In addition, temperature within the porous medium is transferred through channel flow so that temperature distribution in the channel is not stable. Over time, the heating zone in channel flow is still passing through the interface of hot airflow and porous medium, but the zone of instability within the channel is gradually decreased continues to shrink over time. At the final period, the heating zone in channel flow and within the porous medium is changed and the zone of instability is small. It can be seen that the temperature within the porous medium is direct function to time. Fig. 16 shows $t = 600$ s with no external force or in the absence of inlet velocity ($u_i = 0$ m/s). The left side of the temperature distribution is higher temperature than the right because the inlet temperature moves from left to right direction. As explained above, increasing the number of electrodes causes the strength of swirling flow to be greater so that temperature distributions from Figs. 16(b) and (d) are higher than

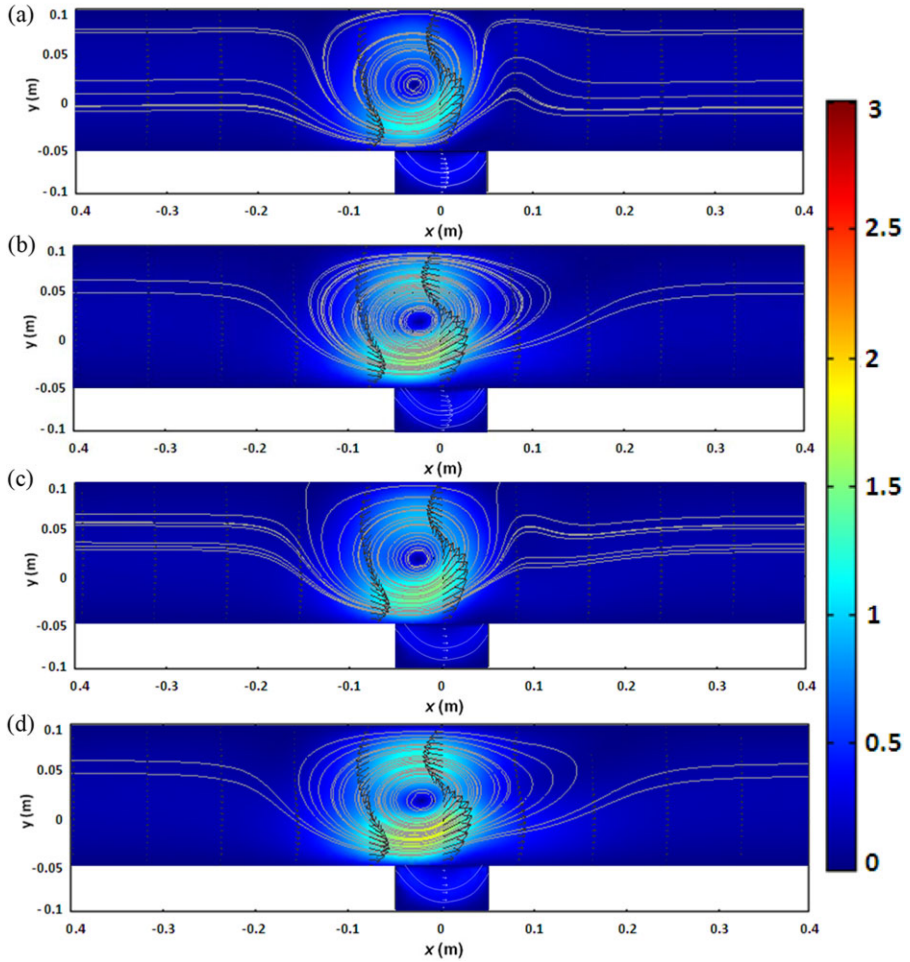

FIGURE 15 Swirling flow (m/s) in a channel flow and fluid flow within porous medium in various row and n: (a) single row ($n = 10$) of aligned configuration, (b) triple rows ($n = 30$) of aligned configuration, (c) single row ($n = 10$) of staggered configuration, and (d) triple rows ($n = 30$) of staggered configuration when $V_0 = 20$ kV and $u_i = 0.1$ m/s [Color figure can be viewed at wileyonlinelibrary.com]

temperature distributions from Figs. 16(a) and (c). Fig. 17 shows $t = 600$ s with external force or inlet velocity ($u_i = 0.1$ m/s). The left side of the temperature distribution is shown to be higher than the right. Depending on the swirling flow, the temperature distribution is demonstrates nonhomogeneous behavior. Due to the conjugate nature of the model, the isotherms are obviously inclined. Its left side is being heated more effectively than the right because swirling flow circulates in the counterclockwise direction, and the lowest temperature is detected on the right side of the sample. The heating zone is increased with increasing number of electrodes, causing her strength of swirling flow so that temperature distributions from Figs. 17(b) and (d) are higher than temperature distributions from Figs. 17(a) and (c). Due to the nonuniform heat flux on sample surface, temperature distribution in the porous medium is not uniform. Therefore, fluid flow above the sample surface is faster and leads to greater heat transfer to the porous medium surface. This causes the temperature of the porous medium to increase rapidly.

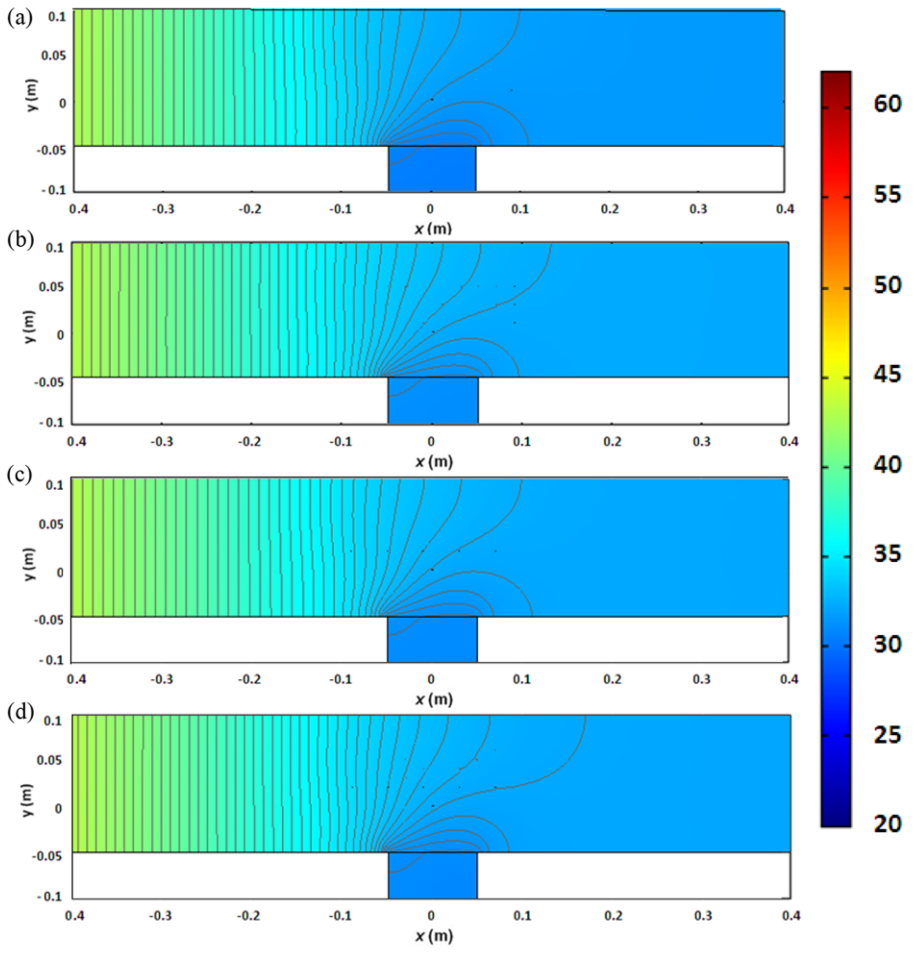

FIGURE 16 Temperature distribution (°C) in various row and n: (a) single row ($n = 10$) of aligned configuration, (b) triple rows ($n = 30$) of aligned configuration, (c) single row ($n = 10$) of staggered configuration, and (d) triple rows ($n = 30$) of staggered configuration when $V_0 = 20$ kV, $u_i = 0$ m/s and $t = 600$ s [Color figure can be viewed at wileyonlinelibrary.com]

When $V_0 = 20$ kV, the average velocity and average temperature within the porous medium between aligned and staggered configurations with various numbers of electrodes are compared in Figs. 18 and 19, respectively. When $u_i = 0$ m/s, average velocity and average temperature within the porous medium are not different, but they are clearly different when $u_i = 0.1$ m/s. The average velocity and average temperature within porous medium of aligned electrode configuration is steeper than in the case of staggered configuration. It can be seen that the average velocity within the porous medium is influenced by average temperature within the porous medium. Therefore, aligned configuration and number of electrodes are dominated with the average velocity within porous medium. The convective heat transfer coefficient ratio within the porous medium using aligned and staggered configurations with various numbers of electrodes is compared in Figs. 20 ($u_i = 0$ m/s) and 21 ($u_i = 0.1$ m/s). The convective heat transfer coefficient ratio is defined as maximum convective heat transfer coefficient with EHD per maximum convective heat transfer coefficient without EHD, that is, $h_{c,EHD}/h_{c,NoEHD}$. As time progresses, the convective heat transfer coefficient ratio has a tendency to decrease. In Fig. 20

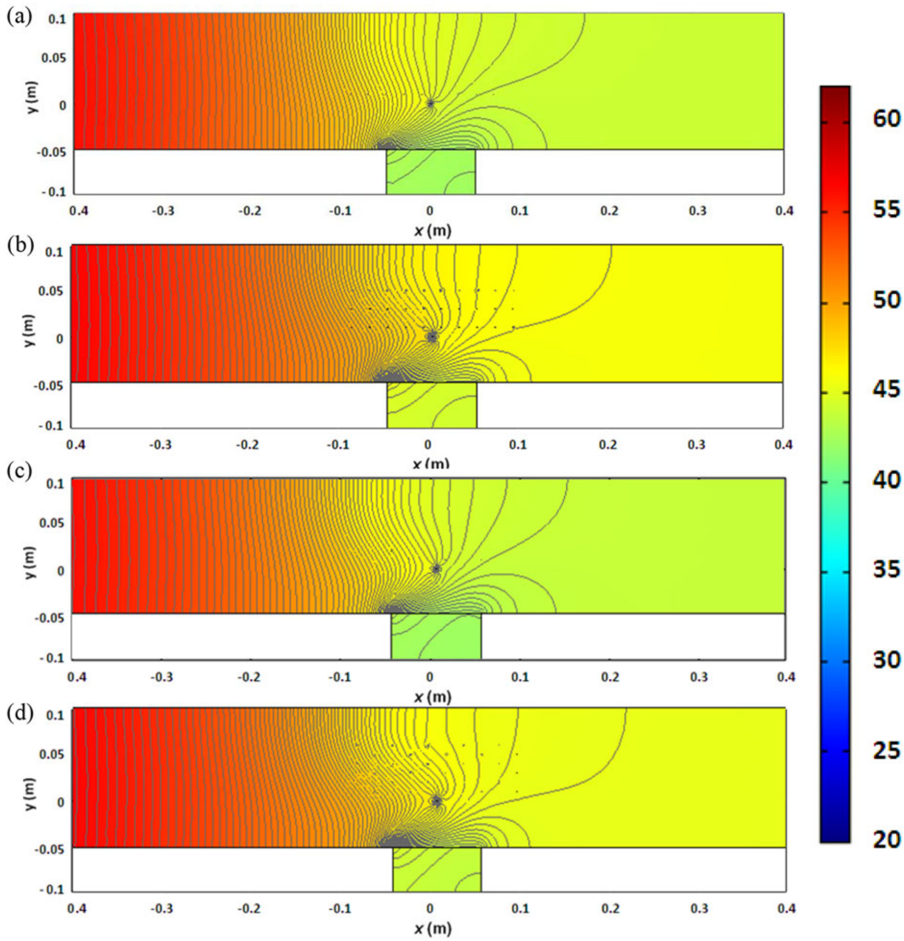

FIGURE 17 Temperature distribution (°C) in various row and n: (a) single row (n = 10) of aligned configuration, (b) triple rows (n = 30) of aligned configuration, (c) single row (n = 10) of staggered configuration, and (d) triple rows (n = 30) of staggered configuration when V_0 = 20 kV, u_i = 0.1 m/s and t = 600 s [Color figure can be viewed at wileyonlinelibrary.com]

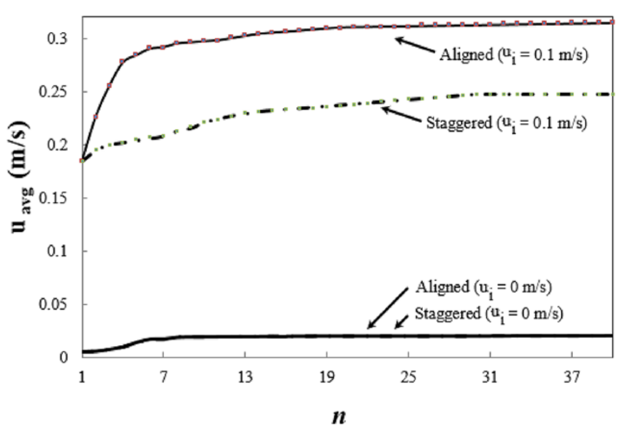

FIGURE 18 Comparison on average velocity within porous medium between aligned and staggered configuration in various number of electrodes when V_0 = 20 kV [Color figure can be viewed at wileyonlinelibrary.com]

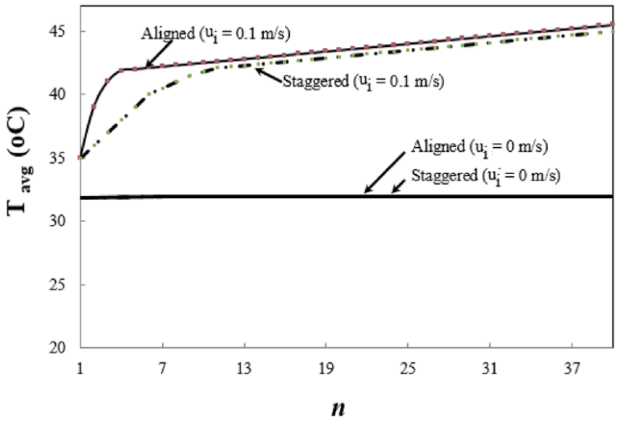

FIGURE 19 Comparison on average temperature within porous medium between aligned and staggered configuration in various number of electrodes when V_0 = 20 kV [Color figure can be viewed at wileyonlinelibrary.com]

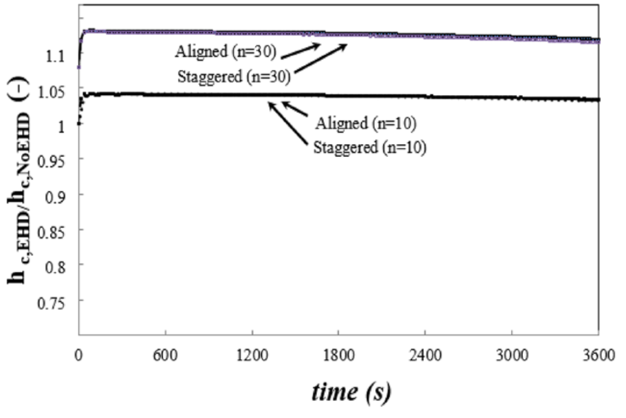

FIGURE 20 Comparison on convective heat transfer coefficient ratio within porous medium between aligned and staggered configuration in various number of electrodes when V_0 = 20 kV and u_i = 0 m/s [Color figure can be viewed at wileyonlinelibrary.com]

(u_i = 0 m/s), the convective heat transfer coefficient ratio within porous medium of n = 30 is higher than n = 10. Increasing the number of electrodes causes different distributions of the convective heat transfer coefficient. Despite that, as shown in Fig. 21 (u_i = 0.1 m/s), the convective heat transfer coefficient ratio within porous medium of aligned configuration is higher than the staggered configuration, and n = 30 is higher than n = 10. In addition, n = 30 and aligned electrode configurations are influenced by the convective heat transfer coefficient ratio. Significant effect of corona wind is observed with aligned configuration and a high number of electrodes. Increasing the number of electrodes can induce electric force more so than electrode arrangement. When V_0 = 20 kV and n = 30, the augmented heat transfer ratios within the porous medium between aligned and staggered configurations are compared in Fig. 22. The augmented heat transfer ratio is defined as maximum Nusselt number with EHD per maximum Nusselt number without EHD, that is, $Nu_{c,EHD}/Nu_{c,NoEHD}$. It can be seen that the augmented heat transfer within porous medium using aligned electrode configuration is slightly lower with time, but the augmented heat transfer within porous medium using staggered configuration is clearly decreased with time. With staggered configurations, the augmented heat transfer within porous medium

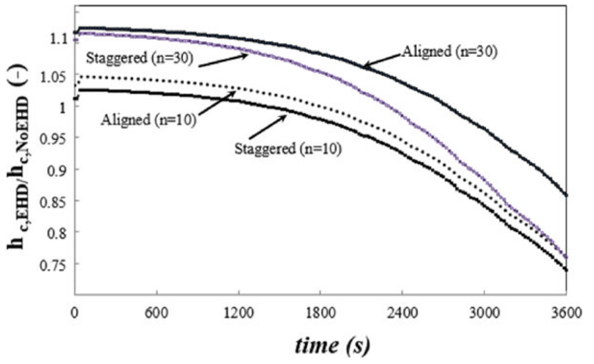

FIGURE 21 Comparison on convective heat transfer coefficient ratio within porous medium between aligned and staggered configuration in various number of electrodes when $V_0 = 20$ kV and $u_i = 0.1$ m/s [Color figure can be viewed at wileyonlinelibrary.com]

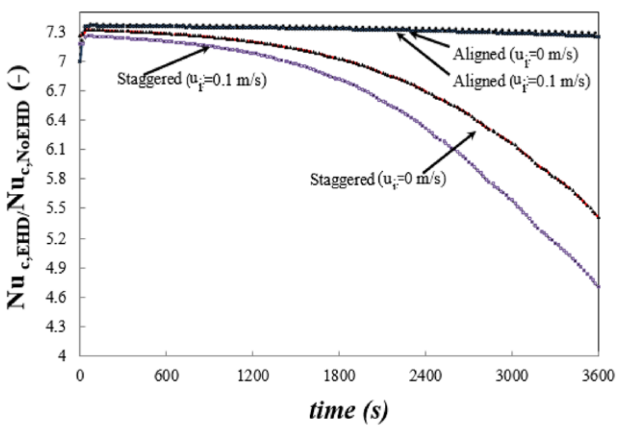

FIGURE 22 Comparison on augmented heat transfer ratio within porous medium between aligned and staggered configuration in various inlet velocity when $V_0 = 20$ kV and $n = 30$ [Color figure can be viewed at wileyonlinelibrary.com]

of $u_i = 0$ m/s is higher than the augmented heat transfer within porous medium of $u_i = 0.1$ m/s. Nevertheless, it appears that with reducing inlet velocity and using the aligned configuration, the augmented heat transfer within porous medium is still high at all time points.

6 | CONCLUSION

Active flow control of electrically driven channel flow is numerically investigated. Also, the effects of electrode bank arrangements and number of electrodes on corona wind and heat transfer enhancement in a porous medium are explored, and we have reached the following conclusions:

First, the electric field effect is induced by shear flow causing swirling flow to appear between the electrode and ground area. The electric force causing shear flow increases the magnitude of the swirling flow. Increasing the number of electrodes causes the electric field to expand and swirling flow to be stronger. Therefore, the swirling flow can induce the fluid flow within porous medium, regardless of time. Moreover, swirling flow causes fluid flow above the sample surface to move faster leading to greater than transfer into the porous medium, resulting rapidly temperature increases and larger heating zones. Increasing the number of electrodes causes different distributions of the convective heat transfer coefficient.

Second, the electric field pattern from staggered electrode configurations is more complicated than that of aligned configurations. The swirling flow zone of staggered configuration is larger than the aligned configuration. Due to the electrode arrangement, the staggered configuration has significantly more induced complexities than aligned configuration, but swirling flow from aligned configuration is more turbulent. Due to higher convective heat transfer on the sample surface, the average velocity and average temperature within a porous medium using aligned configuration is higher than using staggered configuration. The augmented heat transfer within porous medium of aligned configuration is slightly lower with time, but the augmented heat transfer within porous medium using staggered electrode configuration clearly decreases with time.

Finally, it is evident that swirling flow patterns depend on the electrode bank arrangements and number of electrodes. These parameters influence the average velocity within the porous medium. Moreover, increases in the inlet velocity causes the convective heat transfer coefficient ratio and the augmented heat transfer within porous medium to trend lower.

ACKNOWLEDGMENT

The authors would like to gratefully acknowledge the financial support provided by Chulachomklao Royal Military Academy Fund (CRMA Fund) and the Thailand Research Fund (TRF) under the Contract No. TRG5780066 and RTA5980009.

ORCID

Suwimon Saneewong Na Ayuttaya http://orcid.org/0000-0002-7136-996X

REFERENCES

1. Toshiyuki M, Koji S, Kenzo K. Fluid flow and heat transfer of natural convection around large horizontal cylinders: experiments with air. *Heat Trans Asian Res*. 2003;32(4):293–305.
2. Mustafa M, Hayat T, Pop I, Aziz A. Unsteady boundary layer flow of a Casson fluid due to an impulsively started moving flat plate. *Heat Trans Asian Res*. 2011;40(6):563–576.
3. Wintraecken MHMJ, Vegter G. On the optimal triangulation of convex hypersurfaces, whose vertices lie in ambient space. *Math Com Sci*. 2015;9(3):345–353.
4. Yabe A, Mori Y, Hijikata K. EHD study of the corona wind between wire and plate electrodes. *AIAA J*. 1978;16:340–345.
5. Saneewong Na Ayuttaya S, Chaktranond C, Rattanadecho P, Kreewatcharin T. Effect of ground arrangements on swirling flow in a channel subjected to electrohydrodynamics effects. *ASME J Fluids Eng*. 2012;134:051211–9.
6. Sylwia H, Magdalena P. Equalizing calculus in Trefftz method for solving two-dimensional temperature field of FC-72 flowing along the minichannel. *Heat Mass Transf*. 2014;50:1053–1063.
7. Glinov AP. Two-dimensional analysis of the stability of conducting medium flows between permeable plane electrodes inclined to the horizon. *Fluid Dyn*. 2015;50(4):483–493.
8. Lu J, Chu J, Huang W, Ping Z. Preparation of thick Pb(Zr, Ti)O_3 (PZT) film by electrostatic spray deposition (ESD) for application in micro-system technology. *Japanese J Appl Phys*. 2002;41:4317–4320.
9. Jaworek A. Micro- and nanoparticle production by electrospraying. *Power Techol*. 2017;176(1):18–35.
10. Kebarle P, Verkerk UH. Electrospray: from ions in solution to ions in the gas phase, what we know now. *Mass Spectro Rev (Journal Seek)*. 2009;28(6):898–917.

11. Smorodin BL, Taraut AV. Parametric convection of a low-conducting liquid in an alternating electric field. *Fluid Dyns*. 2010;45(1):1–9.
12. Stahnke H, Kittlaus S, Kempe G, Hemmerling C, Aldera L. The influence of electrospray ion source design on matrix effects. *J Mass Spectro*. 2012;47:875–884.
13. Chun YN, Chang JS, Berezin AA, Mizeraczyk J. Numerical modeling of near corona wire electrohydrodynamics flow in a wire-plate electrostatic precipitator. *IEEE Trans Dielectrics Electrical Insulation*. 2007;14(1):119–124.
14. Lin Z, Kazimiers A. Numerical simulation of the electrohydrodynamics flow in a single wire-plate electrostatic precipitator. *IEEE Trans Industry Appl*. 2008;44:683–691.
15. Farnoosh N, Adamiak K, Castle GSP. Three dimensional analysis of electrohydrodynamics flow in a spiked electrode-plate electrostatic precipitator. *J Electrostat*. 2011;69:419–428.
16. Brown NM, Lai FC. Correlations for combined heat and mass transfer from an open cavity in a horizontal channel. *Inter Comm Heat Mass Trans*. 2005;32(8):1000–1008.
17. Bai YX, Sun B. Study of electrohydrodynamics (EHD) drying technique for shrimps. *J Food Process Pres*. 2011;35:891–897.
18. Tang J, Li N, Yu D. Theoretical investigation of operation modes of MHD generators for energy-bypass engines. *J Therm Sci*. 2014;23(6):580–585.
19. Magar YN, Manglik RM. A case study of using enhanced interconnect channel geometries on heat and mass transfer characteristics of anode-supported planar sofc. *J Enhanced Heat Trans*. 2015;22(2):212–215.
20. Fernandez J, Poulter R. Radial mass flow in electrohydrodynamicsally-enhanced forced heat transfer in tubes. *Inter J Heat Mass Trans*. 1987;30(10):2125–2136.
21. Wang FG, Liu YQ, Li RY, Yu HL, Lin ZH. An empirical correlation for EHD enhanced natural convection heat transfer along a plate surface. *J Enhanced Heat Trans*. 2004;11(4):2004.
22. Lai FC, Wang CC. EHD-enhanced water evaporation from partially wetted glass beads with auxiliary heating from below. *Drying Technol*. 2009;27:1199–1204.
23. Kasayapanand N, Kiatsiriroat T. Enhanced heat transfer in partially open square cavities with thin fin by using electric field. *Energy Convers Manage*. 2009;50(2):287–296.
24. Hager WW, Zhang H. A new conjugate gradient method with guaranteed descent and an efficient line search. *SIAM J Optimiz*. 2005;16(1):170–192.
25. Zhang L, Zhou W, Li DH. A descent modified Polak–Ribière–Polyak conjugate gradient method and its global convergence. *IMA J Numer Analy*. 2006;26(4):629–640.
26. He L, Oldfield MLG. Unsteady conjugate heat transfer modeling. *J Turbomach Trans ASME*. 2010;133(3):031022–031033.
27. Tarokh A, Mohamad AA, Jiang L. Simulation of conjugate heat transfer using the lattice Boltzmann method. *Numer Heat Trans Part A Appl Inter J Com Meth*. 2013;63(3):159–178.
28. Landau LD, Lifshitz EM. *Electrohydrodynamics of Continuous Media*. New York: Pergamon; 1963.
29. Klinbun W, Rattanadecho P. Numerical model of microwave driven convection in multilayer porous packed bed using a rectangular waveguide. *Heat Trans Trans ASME*. 2012;134:0426051–042610.
30. COMSOL Inc., COMSOL Multi Physics Modeling Guide.
31. Chun YN, Chang J-S, Berezin AA, Mizeraczyk J. Numerical modeling of near corona wire electrohydrohynamic flow in a wire-plate electrostatic precipitator. *IEEE Trans Dielectric Electrical Insulation*. 2007;14(1):119–124.
32. Sungsoontorn S, Rattanadecho P, Pakdee W. One-dimensional model of heat and mass transports and pressure built-up in unsaturated porous materials subjected to microwave energy. *Drying Technol*. 2011;29:189–204.
33. Saneewong Na Ayuttaya S, Chaktranond C, Rattanadecho P. Numerical analysis of the influence of electrode position on fluid flow in 2-D rectangular duct flow. *J Mech Sci Technol*. 2013;27(7):1957–1962.

How to cite this article: Saneewong Na Ayuttaya S, Chaktranond C, Rattanadecho P. Flow control with electrode bank arrangements by electrohydrodynamics force for heat transfer enhancement in a porous medium. *Heat Transfer—Asian Res*. 2018;47:620–645. https://doi.org/10.1002/htj.21331